Magn Reson Med Sci 2018; 17; 223–230
doi:10.2463/mrms.mp.2017-0094
Published Online: November 16, 2017

MAJOR PAPER

Indirect Proton MR Imaging and Kinetic Analysis of ^{17}O-Labeled Water Tracer in the Brain

Kohsuke Kudo[1,2*], Taisuke Harada[1], Hiroyuki Kameda[1], Ikuko Uwano[2], Fumio Yamashita[2], Satomi Higuchi[2], Kunihiro Yoshioka[3], and Makoto Sasaki[2]

Purpose: The feasibility of steady-state sequences for ^{17}O imaging was evaluated based on a kinetic analysis of the brain parenchyma and cerebrospinal fluid (CSF).

Materials and Methods: The institutional review board approved this prospective study with written informed consent. Dynamic 2D or 3D steady-state sequences were performed in five and nine participants, respectively, with different parameters using a 3T scanner. During two consecutive dynamic scans, saline was intravenously administered for control purposes in the first scan, and 20% ^{17}O-labeled water (1 mL/Kg) was administered in the second scan. Signal changes relative to the baseline were calculated, and kinetic analyses of the curves were conducted for all voxels. Region of interest analysis was performed in the brain parenchyma, choroid plexus, and CSF spaces.

Results: Average signal drops were significantly larger in the ^{17}O group than in the controls for most of the imaging parameters. Different kinetic parameters were observed between the brain parenchyma and CSF spaces. Average and maximum signal drops were significantly larger in the CSF spaces and choroid plexus than in the brain parenchyma. Bolus arrival, time to peak, and the first moment of dynamic curves of ^{17}O in the CSF space were delayed compared to that in the brain parenchyma. Significant differences between the ventricle and subarachnoid space were also noted.

Conclusion: Steady-state sequences are feasible for indirect ^{17}O imaging with reasonable temporal resolution; this result is potentially important for the analysis of water kinetics and aquaporin function for several disorders.

Keywords: *^{17}O, steady state sequence, water kinetics*

Introduction

The ^{17}O isotope is the only stable isotope of oxygen that is capable of producing an MRI signal, with a nuclear magnetic moment γ of 5.7 MHz/Tesla and short T_1/T_2 values[1,2]. As the natural abundance of ^{17}O is only 0.037%, enrichment of ^{17}O is required for MR imaging; however, the enrichment process is expensive. Previous studies have utilized both direct and indirect MRI methods for ^{17}O imaging. The direct method relies on the radiofrequency (RF) of ^{17}O, and both human[3,4] and animal[5,6] studies have been reported; however, it requires specific hardware, such as an amplifier, exciter, and RF coils for ^{17}O.

In contrast, the indirect method relies on the ^{17}O-induced changes in the ^{1}H signal. Therefore, standard clinical MRI machines can be used without any additional hardware. This method utilizes T_2 shortening of ^{17}O-induced proton signals based on scalar coupling between ^{17}O and ^{1}H[2]. For example, to obtain image contrasts using T_2-weighted imaging, a long TE is required in fast spin echo sequences. However, the brain parenchyma becomes too dark with a long TE, making it difficult to determine the signal change. Therefore, indirect ^{17}O imaging has been mostly conducted using T_1-ρ or decoupling sequences[7–10], although such methods remain relatively uncommon, and the decoupling sequence requires a specific RF coil for ^{17}O, similar to the direct method. Further, no human research has been conducted using the indirect method.

Steady-state sequences have been used in conjunction with long scan times for high-resolution cisternography

[1]Department of Diagnostic and Interventional Radiology, Hokkaido University Hospital, N14 W5 Kita-ku, Sapporo, Hokkaido 060-8648, Japan
[2]Division of Ultrahigh Field MRI, Institute for Biomedical Sciences, Iwate Medical University, Iwate, Japan
[3]Department of Radiology, Iwate Medical University, Iwate, Japan
*Corresponding author, Phone: +81-11-706-5977, Fax: +81-11-706-7876, E-mail: kkudo@huhp.hokudai.ac.jp

Received: July 13, 2017 | Accepted: September 14, 2017

based on their strong T_2 contrast. We hypothesized that modifying imaging parameters would allow for dynamic steady-state indirect imaging of ^{17}O with reasonable temporal resolution.

The purpose of the present study was to evaluate the feasibility of steady-state sequences for ^{17}O imaging via kinetic analysis of the brain parenchyma and cerebrospinal fluid (CSF) following administration of a ^{17}O water tracer.

Materials and Methods

Participants

After the Institutional Review Board of our institution approved our study protocol, we recruited male volunteers with no past history of neurological disease from December 2012 to February 2015. The inclusion criteria included an age between 20 and 65 years old, and a body weight below 60 kg. Fourteen male volunteers (mean age: 28.6 years; age range: 21–39 years) were eligible. Written informed consent was obtained from all participants prior to enrollment in our study.

Magnetic resonance imaging

MRI scans were conducted using a 3.0 Tesla scanner (MR750; GE Healthcare, Milwaukee, WI, USA) with an 8-channel head coil. After the scout scan, dynamic 2D or 3D scans were performed with fast imaging employing steady state acquisition (FIESTA) sequences with variable parameters (Table 1). Five and nine participants underwent 2D and 3D imaging, respectively.

Single section acquisition with high flip angle (flip angle [FA], 90 degrees) and long repetition time (TR, 32.6 to 42.6 ms)/echo time (TE, 30 to 40 ms) were used for 2D imaging, with the section location at the centrum semiovale. For 3D imaging, low FA and short TR/TE, high FA and short TR/TE, and high FA and long TR/TE were respectively applied to three participants. The middle of the scan slab was set at the level of the basal ganglia. The total scan time was approximately 6 minutes.

Two consecutive dynamic scans were performed for each participant. In the first dynamic scan, saline (1 mL/kg weight) was intravenously administered 60 or 120 s after the start of scanning for control purposes via the antecubital vein at a rate of 3 mL/s. In the second dynamic scan, ^{17}O-labeled water (enriched to 20%; Taiyo Nippon Sanso Corp, Tokyo, Japan) was administered at the same dose, timing, and rate. This water tracer was made with good manufacturing practice (GMP) standards for intravenous injection in human participants.

Data analysis

The acquired image data were post-processed with in-house software (Perfusion Mismatch Analyzer [PMA] Research Version 5.2.0.1; Acute Stroke Imaging Standardization Group, Tokyo, Japan). Relative signals to the average baseline were calculated for all voxels, and the dynamic curves were analyzed. To exclude the unstable signals, the first 15 s data was discarded and the baseline was defined between 15 s after the scan start and the injection point of saline or ^{17}O-labeled water. Gaussian smoothing was applied for the temporal axis (the sigma of which was 10 s), and data interpolation was not used. No spatial smoothing was applied to avoid the contamination of signal changes from adjacent voxels.

The average signal drop (ASD) was calculated within the period from the injection start of saline or ^{17}O-labeled water to the end of the scan. Other kinetic parameters such as bolus arrival time (BAT), time to peak (TTP), first moment (FM), and maximum signal drop (MSD) were also calculated voxel by voxel. BAT was defined as the time at which a signal drop larger than 5% of maximum occurred. TTP was defined as the time of bolus peak, while FM was defined as the first moment of bolus area (gravity center).

ROI analysis was performed using the same software (Fig. 1). Ten square ROIs were manually defined in the cerebral cortex (CC), basal ganglia/thalamus (BG/TM), white matter (WM), choroid plexus (CP), ventricles, and subarachnoid space (SAS), respectively. To avoid the contamination of signal changes between CC and SAS, and between CP and ventricle, small size of ROI (4×4 mm) was used. In addition, 10 ROIs were evenly placed and banding artifact of FIESTA sequence was carefully avoided. ASD, BAT, TTP, FM, and MSD were measured for each of these ROIs. However, these values were not measured in the BG/TM, CP, and ventricles of five, four, and two participants who underwent 2D imaging, respectively, because those structures were not included within the section.

Statistical analysis

The ASDs of the ^{17}O-enriched water and saline control conditions were compared using paired t-tests for each location in each participant to assess whether a significant signal drop caused by T_2 shortening of ^{17}O-enriched water had occurred. For participants in whom significant differences in the ASD were noted, we then compared the kinetic parameters of ^{17}O-enriched water in each location using an analysis of variance followed by multiple comparisons using the Holm-Sidak method. A *P*-value less than 0.05 was considered significant in all statistical tests.

Results

All participants completed the study protocol, and no adverse effects were noted following the intravenous administration of ^{17}O-enriched water.

In 2D imaging, the ASD of the CC, CP, ventricles, and SAS were significantly larger in the ^{17}O than control condition for all participants (Table 2). Four of five participants also exhibited significant differences in ASD of WM. In 3D imaging, there were no significant differences in ASD at any location for any participant of the low FA and short TR/TE

Table 1. Imaging parameters

Imaging sequence			No.	FA	TR (ms)	TE (ms)	Matrix	NEX	No. of section	Section thickness (mm)	No. of dynamic phase	Temporal resolution (sec)	FOV (mm)	Phase FOV	Total scan time (sec)
2D			1	90	32.6	30.0	256 × 128	1	1	5	77	4.7	240 × 180	0.75	363
			2	90	42.6	40.0	256 × 128	1	1	5	54	6.8	240 × 180	0.75	369
			3	90	42.6	40.0	256 × 128	1	1	5	62	5.8	240 × 180	0.75	362
			4	90	42.3	40.0	256 × 128	2	1	5	28	13.4	240 × 180	0.75	376
			5	90	42.3	40.0	256 × 128	4	1	5	15	24.3	240 × 180	0.75	365
3D	Low	Short	6	5	2.8	1.4	128 × 128	1	12	5	110	3.3	240 × 180	0.75	362
	FA	TR/TE	7	20	2.4	0.9	128 × 128	1	28	5	74	4.8	240 × 180	0.75	354
			8	25	2.8	1.4	128 × 128	1	12	5	110	3.3	240 × 180	0.75	362
	High	Short	9	70	3.2	1.5	128 × 90	0.75	40	4	120	3.0	240 × 180	0.75	356
	FA	TR/TE	10	70	3.2	1.5	128 × 128	1	20	4	24	15.1	240 × 180	0.75	362
			11	90	11.1	5.4	512 × 128	1	4	14	20	19.0	240 × 192	0.8	379
		Long	12	90	21.3	20.0	128 × 128	1	4	10	23	16.0	320 × 160	0.5	367
		TR/TE	13	90	31.4	30.0	128 × 64	0.75	4	14	22	16.5	240 × 180	0.75	362
			14	90	51.3	50.0	128 × 64	1	4	14	11	35.0	300 × 180	0.6	385

FA, flip angle; NEX, number of excitation.

value group. In the high FA and short TR/TE group, significant differences in ASD were noted in two, one, two, three, and three participants for the CC, WM, CP, ventricle, and SAS, respectively. No significant differences were observed in the BG/TM for any of the three participants. In the high FA and long TR/TE group, significant differences were observed in all locations in all participants.

As no significant differences were noted in any participant of the low FA and short TR/TE group, these three participants were excluded from the following analysis of kinetic parameters. Examples of parameter maps and dynamic curves in a single participant are shown in Figs. 2 and 3, respectively.

The kinetic parameters of eleven participants are summarized in Fig. 4. Significantly larger BAT values were observed for the ventricles and SAS relative to other locations, indicating that bolus arrivals of ^{17}O in the CSF space were delayed compared to the brain parenchyma. Similarly, TTP and FM of the ventricles and SAS were significantly larger than values in other locations. In addition, TTP values of the CP were significantly larger than those of the CC and BG/TM. WM exhibited slightly but significantly larger TTP values than the BG/TM. FM values of the BG/TM were significantly smaller than those in other locations, with the exception of the CC.

MSD and ASD values in the SAS, ventricles, and CP were significantly larger than those in other locations. Among these, values for the SAS were significantly higher than those for the CP and ventricles, while values for the CP were

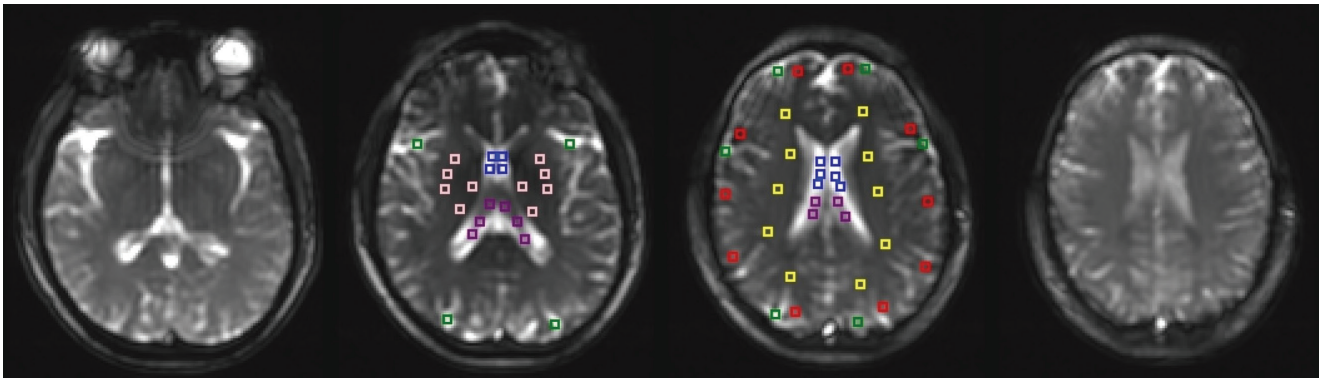

Fig. 1 Regions of interest. Ten square ROIs (4 mm x 4 mm) are defined in the cerebral cortex (red), basal ganglia/thalamus (pink), white matter (yellow), choroid plexus (purple), ventricles (blue), and subarachnoid space (green).

Table 2. Difference of ASD between ^{17}O and control

			No.	Cerebral cortex			Basal ganglia/thalamus			White matter		
				^{17}O	Control	*P* value	^{17}O	Control	*P* value	^{17}O	Control	*P* value
2D			1	1.9 ± 1.1	−0.3 ± 0.9	< 0.001	N.A.	N.A.	N.A.	0.4 ± 0.4	−0.3 ± 0.3	< 0.01
			2	2.5 ± 1.5	−0.1 ± 1.1	< 0.001	N.A.	N.A.	N.A.	2.3 ± 2.0	−0.2 ± 0.7	< 0.05
			3	4.3 ± 3.6	0.3 ± 1.8	< 0.01	N.A.	N.A.	N.A.	0.6 ± 0.8	−0.8 ± 0.6	< 0.05
			4	9.4 ± 3.0	1.1 ± 5.3	< 0.01	N.A.	N.A.	N.A.	0.6 ± 1.4	−1.6 ± 1.3	< 0.01
			5	3.1 ± 1.7	−0.7 ± 1.1	< 0.001	N.A.	N.A.	N.A.	1.4 ± 0.7	0.3 ± 1.5	N.S.
3D	Low	Short	6	0.5 ± 0.5	0.4 ± 0.4	N.S.	0.4 ± 0.2	0.4 ± 0.2	N.S.	0.4 ± 0.3	0.3 ± 0.3	N.S.
	FA	TR/TE	7	0.8 ± 1.3	0.7 ± 0.5	N.S.	0.2 ± 0.6	0.5 ± 0.6	N.S.	0.2 ± 0.6	0.1 ± 0.7	N.S.
			8	0.1 ± 0.5	−0.2 ± 0.4	N.S.	0.7 ± 0.5	0.7 ± 0.3	N.S.	0.3 ± 0.4	−0.2 ± 0.8	N.S.
	High	Short	9	−0.5 ± 0.5	−0.3 ± 0.6	N.S.	−0.1 ± 2.5	−2.4 ± 3.1	N.S.	−0.6 ± 1.2	−0.8 ± 0.9	N.S.
	FA	TR/TE	10	1.6 ± 1.6	−0.9 ± 0.6	< 0.001	1.8 ± 4.1	1.9 ± 3.0	N.S.	2.8 ± 2.4	0.1 ± 1.7	N.S.
			11	1.9 ± 1.2	−0.3 ± 0.5	< 0.001	1.9 ± 1.5	1.0 ± 2.1	N.S.	1.8 ± 1.0	−0.1 ± 1.2	< 0.01
		Long	12	5.9 ± 2.0	0.0 ± 0.7	< 0.001	1.2 ± 0.9	−0.3 ± .9	< 0.01	1.2 ± 0.8	−0.3 ± 1.4	< 0.05
		TR/TE	13	4.2 ± 1.2	−0.6 ± 0.7	< 0.001	1.9 ± 1.5	0.1 ± 2.5	< 0.05	1.3 ± 2.0	−1.2 ± 2.0	< 0.05
			14	5.9 ± 4.6	−2.5 ± 3.7	< 0.001	7.4 ± 3.0	0.8 ± 3.6	< 0.001	5.0 ± 4.0	0.6 ± 3.8	< 0.05

N.A., not applicable; N.S., not significant.

significantly higher than those in the ventricles. ASD and MSD values were significantly smaller in the WM than in the CC. Significantly larger MSD values were noted in the SAS when compared to those of the ventricles and BG/TM. Furthermore, the ventricle exhibited significantly smaller MSD values than the CC.

Discussion

In the present study, we applied steady-state sequences for the indirect imaging of ^{17}O. Steady-state imaging is usually applied for high-resolution hydrography; however, we reduced the spatial resolution to achieve a reasonable temporal resolution for the evaluation of dynamic signal changes following the administration of ^{17}O water tracer. Although dependencies in scan parameters existed, significant ^{17}O-induced signal drops were observed using both 2D and 3D steady-state imaging.

Steady-state sequences rely on T_2/T_1 contrast and are usually used with a short TR/TE to reduce the influence of banding artifacts[11]. Better temporal resolution (3.3–4.8 s) was obtained with short TR/TE in 3D imaging; however, no significant signal drops of ^{17}O were observed. In contrast, significant signal drops in ^{17}O were observed using a long TR/TE in conjunction with a high FA. Although temporal resolution became longer with a longer TR, this combination of parameters could be effectively used for indirect ^{17}O imaging. Other sequences such as fast spin echo, echo planar imaging (EPI), and gradient echo are potential candidates for T_2-weighted imaging of ^{17}O. However, a longer TR/TE may be required to obtain T_2 contrast of ^{17}O, which may result in a significant signal drop before the administration of ^{17}O in the brain parenchyma, a lower signal-to-noise ratio, and a decreased temporal resolution.

In the present study, signal changes (ASD and MSD) in CC were significantly larger than in WM. Although quantification has not been conducted, these differences in signal change may reflect the difference of cerebral blood flow and/or volume. In CT and MR perfusion study, Cerebral blood flow can be measured by maximum slope model; however, there was no significant differences in MS between CC and WM. This was probably because we used diffusible tracer which is different from intravascular tracer of CT perfusion (iodine contrast) and MR perfusion (Gd contrast). In addition, MS calculation might be susceptible to image noise as the signal change is too small to measure, while ASD and MSD were relatively robust to noise as these parameters were simply calculated as the average or maximum of signals.

Signal changes in the CSF were larger than brain parenchyma, likely because ^{17}O is a water tracer, and difference in relaxation time between brain parenchyma and CSF. Such a result has not been observed using ^{15}O positron emission tomography (PET), probably because of the larger signal change with ^{17}O MRI in CSF, or due to the short half-life of ^{15}O which leaks out to the CSF. In contrast, ^{17}O is a stable isotope, allowing for the visualization of a relatively slower water leakage from vessels or brain parenchyma into the CSF space, such as the ventricles and SAS, compared to a faster blood flow. In the classic theory, the choroid plexus produces CSF;

Table 2. Continued

Choroid plexus			Ventricle			Subarachnoid space		
^{17}O	Control	*P* value	^{17}O	Control	*P* value	^{17}O	Control	*P* value
N.A.	N.A.	N.A.	N.A.	N.A.	N.A.	4.3 ± 1.6	−0.4 ± 0.6	< 0.001
N.A.	N.A.	N.A.	N.A.	N.A.	N.A.	8.1 ± 2.3	0.3 ± 1.0	< 0.001
7.3 ± 2.8	0.6 ± 0.5	< 0.001	5.7 ± 2.0	0.1 ± 1.5	< 0.001	11.0 ± 3.0	−0.2 ± 1.5	< 0.001
N.A.	N.A.	N.A.	2.6 ± 1.6	−0.6 ± 1.1	< 0.01	8.5 ± 2.8	−2.3 ± 4.1	< 0.001
N.A.	N.A.	N.A.	2.0 ± 1.8	−0.5 ± 1.2	< 0.01	5.5 ± 2.0	−0.3 ± 0.6	< 0.001
0.5 ± 0.2	0.3 ± 0.3	N.S.	0.4 ± 0.3	0.1 ± 0.4	N.S.	0.3 ± 0.4	0.2 ± 0.3	N.S.
0.4 ± 0.9	1.0 ± 1.0	N.S.	1.3 ± 1.3	0.8 ± 1.0	N.S.	0.7 ± 1.0	0.7 ± 1.0	N.S.
0.1 ± 2.1	−0.4 ± 2.0	N.S.	−1.1 ± 3.5	0.8 ± 3.0	N.S.	0.6 ± 1.0	1.2 ± 0.9	N.S.
0.1 ± 6.2	3.5 ± 6.6	N.S.	6.1 ± 5.7	−4.5 ± 6.1	< 0.05	4.1 ± 1.5	−0.6 ± 3.1	< 0.001
3.7 ± 2.4	−0.1 ± 0.6	< 0.001	5.0 ± 1.5	−0.2 ± 0.7	< 0.001	4.6 ± 1.9	0.5 ± 0.5	< 0.001
8.1 ± 1.6	0.3 ± 1.3	< 0.001	6.6 ± 1.7	0.6 ± 1.4	< 0.001	8.2 ± 1.5	−0.8 ± 0.7	< 0.001
8.7 ± 2.3	0.1 ± 0.6	< 0.001	5.0 ± 1.1	0.0 ± 0.8	< 0.001	12.6 ± 2.6	−0.1 ± 1.0	< 0.001
8.5 ± 3.7	0.5 ± 0.7	< 0.001	3.6 ± 1.3	0.7 ± 1.2	< 0.001	9.4 ± 1.2	−0.4 ± 0.9	< 0.001
9.8 ± 5.5	0.7 ± 1.8	< 0.001	6.4 ± 2.8	−1.7 ± 2.6	< 0.001	12.0 ± 1.8	−1.0 ± 2.2	< 0.001

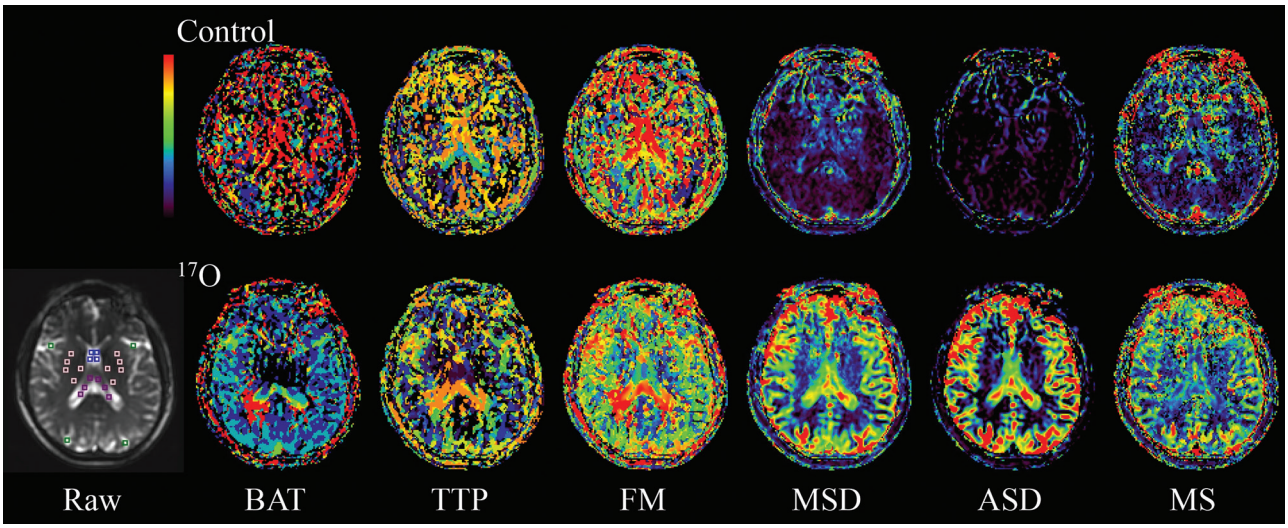

Fig. 2 Parameter maps. Examples of parameter maps (3D imaging with a high FA and a long TR/TE) are shown. In ^{17}O maps, higher ASD and MSD values are observed in the subarachnoid space, choroid plexus, and cerebral cortex when compared to the saline control condition. Time-related parameters such as BAT, TTP, and FM are noisy; however, some anatomical structures are more easily visualized following ^{17}O injection when compared to saline control conditions. BAT, bolus arrival time; TTP, time to peak; FM, first moment; MSD, maximum signal drop; ASD, average signal drop; MS, maximum slope; FA, flip angle.

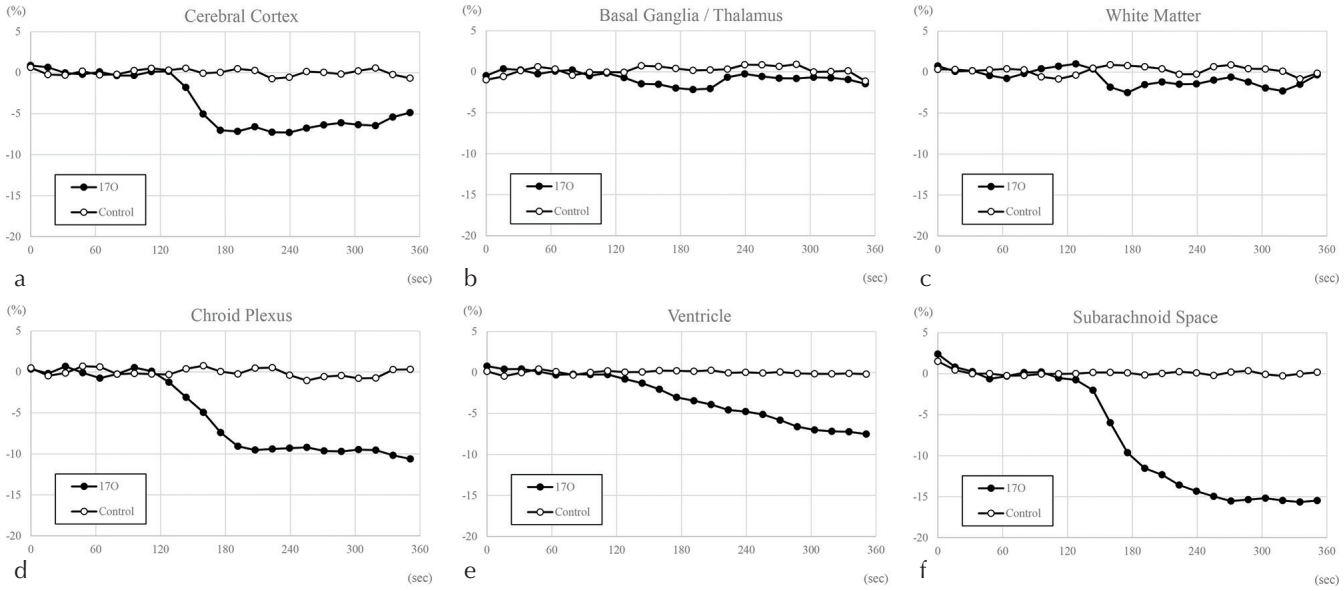

Fig. 3 Dynamic curves of relative signals. Examples of dynamic curves in a single participant (same as Fig. 2) are shown. The bolus injection of saline or ^{17}O is initiated 120 s after the scan start. Significant signal drops are observed in the cerebral cortex (**a**), choroid plexus (**d**), ventricle (**e**), and subarachnoid space (**f**) in the ^{17}O condition, while slight decreases in the signals are noted in the basal ganglia/thalamus (**b**) and white matter (**c**). In the cerebral cortex, choroid plexus, and subarachnoid space, the curves are characterized by two phases, i.e., an initial signal drop phase and a plateau phase. In the ventricle, the signals gradually and continuously decreased during the acquisition time window.

however, in our study, earlier and more rapid signal changes were observed in the SAS compared to the ventricle, indicating fluid leakage from vessels or the surface of the brain. This observation is compatible with the findings of previous studies that used ^{17}O as a water tracer[12]; therefore, we conclude that ^{17}O can be used as a tracer in the analysis of CSF kinetics.

Previous studies have indicated that aquaporin (AQP) may be associated with the pathogenesis of several diseases. For example, neuromyelitis optica (NMO) is associated with antibodies to AQP[13]. Additional studies have reported that Alzheimer's disease and Parkinson's disease are associated with changes in the expression of AQP[14–16].

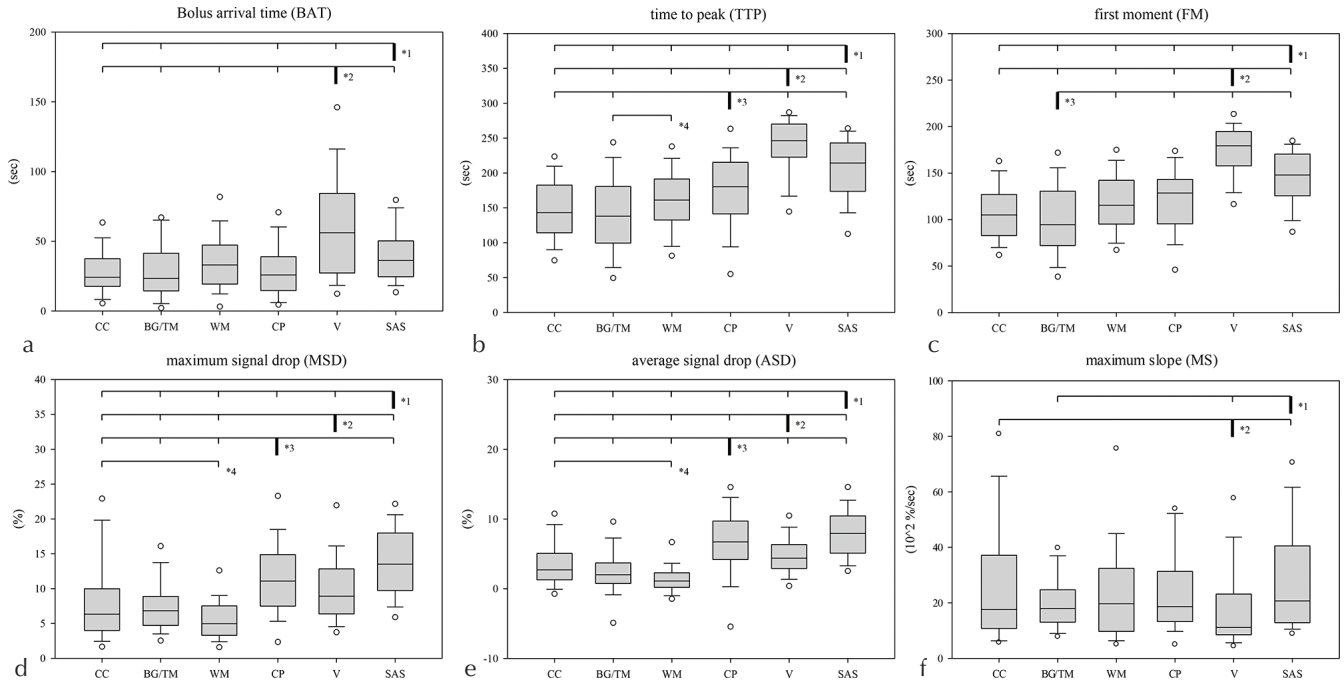

Fig. 4 Comparisons of kinetic parameters among locations. The kinetic parameters of 11 participants are summarized. Three participants are excluded due to no significant signal drops following injection of ^{17}O. Significant differences ($P < 0.05$) are indicated with an asterisk (*) and a bold line as a reference. For example, significant differences in BAT are observed for the SAS when compared with the cerebral cortex, basal ganglia/thalamus, choroid plexus, and ventricles, although no such differences are noted when this region is compared with the white matter. BAT (**a**), TTP (**b**), and FM (**c**) of the ventricle and SAS are significantly larger than the brain parenchyma. Similarly, MSD (**d**) and ASD (**e**) of the choroid plexus, ventricle, and SAS are significantly larger than the brain parenchyma. MS (**f**) of the SAS is significantly larger than the ventricle, indicating rapid signal change. BG, basal ganglia; CC, cerebral cortex; CP, choroid plexus; SAS, subarachnoid space; TM, thalamus; WM, white matter.

Other brain disorders such as stroke, intracranial hematoma, and edema may also be related to AQP function[17–20]. In addition to the central nervous system, altered expression of AQP has been noted in several diseases in the lungs, kidneys, liver, and other organs[21–24]. Although the distribution of AQP can be histologically analyzed, the dynamic function of AQP *in vivo* cannot be evaluated without the use of a water tracer. Currently, no tracers have been useful for AQP kinetics analysis; however, our findings indicate that ^{17}O may be one such candidate for use in MR imaging. The dysfunction of AQP channel might be imaged with ^{17}O-water as decreased signal change of impaired lesion.

The present study has several limitations. First, the temporal and spatial resolution was not high enough, especially for a longer TR/TE, and a much higher resolution may be required for a detailed examination of water kinetics in small structures of the brain. Second, a longer TR/TE may produce strong banding artifacts. Therefore, improved homogeneity of the static magnetic field may be required. Third, contamination of signal change between CC and SAS, and between CP and ventricle might be occurred even we used small ROI. Although we carefully avoided the location of banding artifact of FIESTA sequence, several ROIs may suffer signal decrease derived from banding artifact Furthermore, although we observed significant changes in relative signals, we did not quantify the absolute amount of ^{17}O. Further studies are required for such quantification, although our results have revealed significant differences in the kinetics of dynamic curves using relative signal changes.

Conclusion

Our findings indicate that steady-state sequences are feasible for indirect ^{17}O imaging with reasonable temporal resolution; this result is potentially important for the analysis of water kinetics and AQP function for several disorders.

Acknowledgments

This work was supported in part by a Grant-in-Aid for Strategic Medical Science Research from the Ministry of Education, Culture, Sports, Science and Technology of Japan, and by the Japan Society for the Promotion of Science (JSPS) through the "Funding Program for Next Generation World-Leading Researchers (NEXT Program)" initiated by the Council for Science and Technology Policy (CSTP).

Conflicts of Interest

No financial interests.

References

1. Gordji-Nejad A, Möllenhoff K, Oros-Peusquens AM, Pillai DR, Shah NJ. Characterizing cerebral oxygen metabolism employing oxygen-17 MRI/MRS at high fields. MAGMA 2014; 27:81–93.
2. Zhu XH, Zhang N, Zhang Y, Zhang X, Ugurbil K, Chen W. *In vivo* ^{17}O NMR approaches for brain study at high field. NMR Biomed 2005; 18:83–103.
3. Hoffmann SH, Radbruch A, Bock M, Semmler W, Nagel AM. Direct ^{17}O MRI with partial volume correction: first experiences in a glioblastoma patient. MAGMA 2014; 27:579–587.
4. Atkinson IC, Thulborn KR. Feasibility of mapping the tissue mass corrected bioscale of cerebral metabolic rate of oxygen consumption using ^{17}-oxygen and 23-sodium MR imaging in a human brain at 9.4 T. Neuroimage 2010; 51:723–733.
5. Cui W, Zhu XH, Vollmers ML, et al. Non-invasive measurement of cerebral oxygen metabolism in the mouse brain by ultra-high field ^{17}O MR spectroscopy. J Cereb Blood Flow Metab 2013; 33:1846–1849.
6. Zhu XH, Zhang Y, Zhang N, Ugurbil K, Chen W. Noninvasive and three-dimensional imaging of $CMRO_2$ in rats at 9.4 T: reproducibility test and normothermia/hypothermia comparison study. J Cereb Blood Flow Metab 2007; 27:1225–1234.
7. Tailor DR, Roy A, Regatte RR, et al. Indirect ^{17}O-magnetic resonance imaging of cerebral blood flow in the rat. Magn Reson Med 2003; 49:479–487.
8. Tailor DR, Poptani H, Glickson JD, Leigh JS, Reddy R. High-resolution assessment of blood flow in murine RIF-1 tumors by monitoring uptake of H_2 ^{17}O with proton $T_{1\rho}$-weighted imaging. Magn Reson Med 2003; 49:1–6.
9. de Crespigny AJ, D'Arceuil HE, Engelhorn T, Moseley ME. MRI of focal cerebral ischemia using (17)O-labeled water. Magn Reson Med 2000; 43:876–883.
10. Ronen I, Merkle H, Ugurbil K, Navon G. Imaging of H_2 ^{17}O distribution in the brain of a live rat by using proton-detected ^{17}O MRI. Proc Natl Acad Sci USA 1998; 95:12934–12939.
11. Björk M, Ingle RR, Gudmundson E, Stoica P, Nishimura DG, Barral JK. Parameter estimation approach to banding artifact reduction in balanced steady-state free precession. Magn Reson Med 2014; 72:880–892.
12. Igarashi H, Tsujita M, Kwee IL, Nakada T. Water influx into cerebrospinal fluid is primarily controlled by aquaporin-4, not by aquaporin-1: ^{17}O JJVCPE MRI study in knockout mice. Neuroreport 2014; 25:39–43.
13. Saikali P, Cayrol R, Vincent T. Anti-aquaporin-4 autoantibodies orchestrate the pathogenesis in neuromyelitis optica. Autoimmun Rev 2009; 9:132–135.
14. Potokar M, Jorgačevski J, Zorec R. Astrocyte aquaporin dynamics in health and disease. Int J Mol Sci 2016;17: 1121. doi:10.3390/ijms17071121
15. Lan YL, Zhao J, Ma T, Li S. The potential roles of aquaporin 4 in Alzheimer's disease. Mol Neurobiol 2016; 53: 5300–5309.
16. Sun H, Liang R, Yang B, et al. Aquaporin-4 mediates communication between astrocyte and microglia: Implications of neuroinflammation in experimental Parkinson's disease. Neuroscience 2016; 317:65–75.
17. Zhang YW, Li HT, Hu J, Lin Y, Hou JM, Wu WJ. [Correlation analysis between the expression of aquaporin 4 and magnetic resonance imaging of brain tissue in severely scalded rabbit with brain edema during early stage]. Zhonghua Shao Shang Za Zhi 2011; 27:441–445. (in Chinese)
18. Badaut J, Ashwal S, Tone B, Regli L, Tian HR, Obenaus A. Temporal and regional evolution of aquaporin-4 expression and magnetic resonance imaging in a rat pup model of neonatal stroke. Pediatr Res 2007; 62:248–254.
19. Chiu CD, Chen CC, Shen CC, et al. Hyperglycemia exacerbates intracerebral hemorrhage via the downregulation of aquaporin-4: temporal assessment with magnetic resonance imaging. Stroke 2013; 44:1682–1689.
20. Brissaud O, Villega F, Pieter Konsman J, et al. Short-term effect of erythropoietin on brain lesions and aquaporin-4 expression in a hypoxic-ischemic neonatal rat model assessed by magnetic resonance diffusion weighted imaging and immunohistochemistry. Pediatr Res 2010; 68:123–127.
21. Choma DP, Vanacore R, Naylor H, et al. Aquaporin 11 variant associates with kidney disease in type 2 diabetic patients. Am J Physiol Renal Physiol 2016; 310:F416–F425.
22. Hansel NN, Sidhaye V, Rafaels NM, et al. Aquaporin 5 polymorphisms and rate of lung function decline in chronic obstructive pulmonary disease. PLoS ONE 2010; 5:e14226.
23. Gena P, Mastrodonato M, Portincasa P, et al. Liver glycerol permeability and aquaporin-9 are dysregulated in a murine model of Non-Alcoholic Fatty Liver Disease. PLoS ONE 2013; 8:e78139.
24. Hodeib A, Hegab D, Rizk O, Mohammed S. Immunohistochemical expression of AQP-3 in vitiligo; a new potential guide for disease activity. G Ital Dermatol Venereol 2017; 152:348–354.